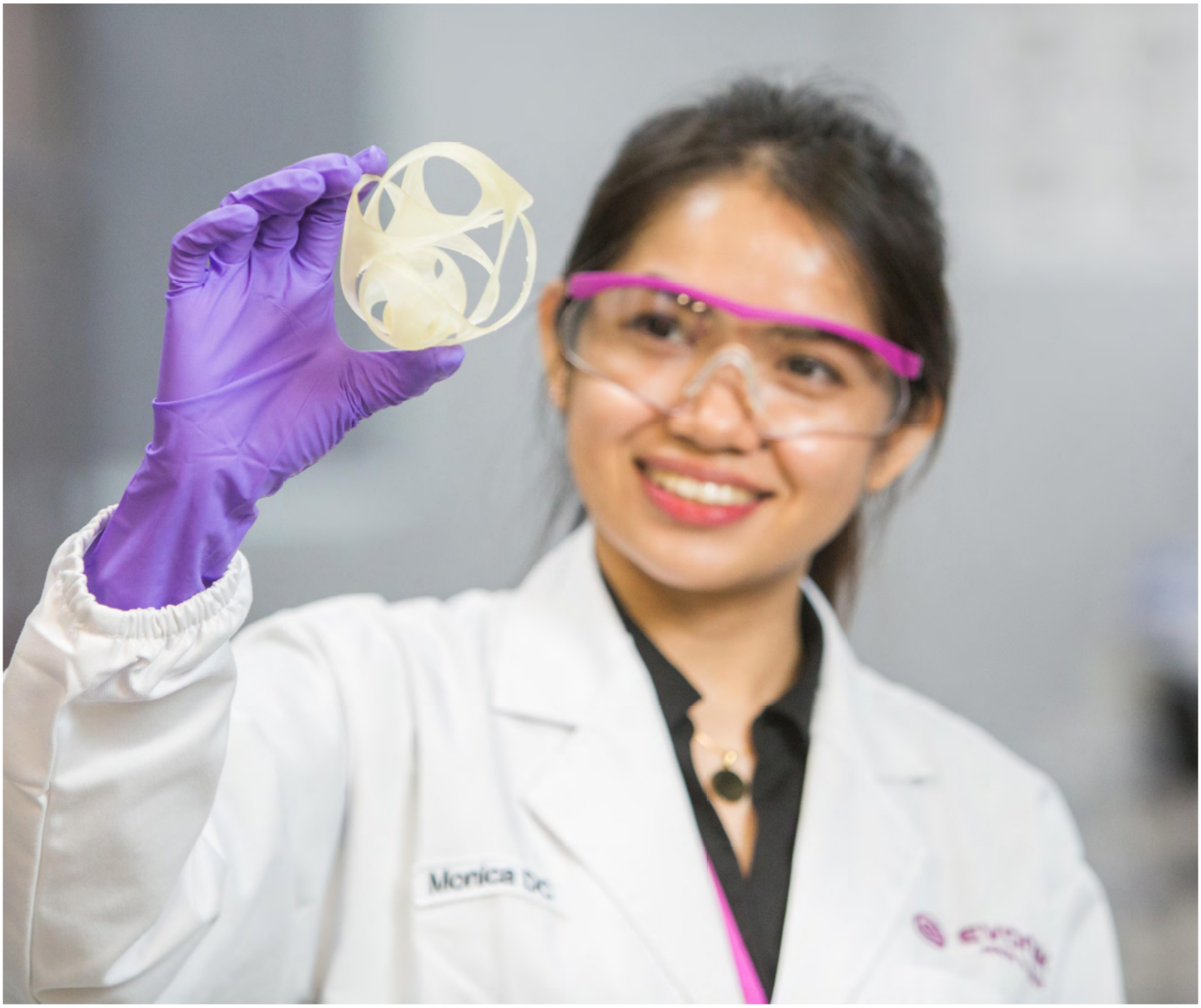
Monica

ADVANCED FUNCTIONAL MATERIALS
www.afm-journal.de

Decomposition of Trace Li_2CO_3 During Charging Leads to Cathode Interface Degradation with the Solid Electrolyte LLZO

*Alexander A. Delluva, Jonas Kulberg-Savercool, and Adam Holewinski**

A major challenge for lithium-containing electrochemical systems is the formation of lithium carbonates. Solid-state electrolytes circumvent the use of organic liquids that can generate these species, but they are still susceptible to Li_2CO_3 formation from exposure to water vapor and carbon dioxide. It is reported here that trace quantities of Li_2CO_3, which are re-formed following standard mitigation and handling procedures, can decompose at high charging potentials and degrade the electrolyte–cathode interface. Operando electrochemical mass spectrometry (EC–MS) is employed to monitor the outgassing of solid-state batteries containing the garnet electrolyte $Li_7La_3Zr_2O_{12}$ (LLZO) and using appropriate controls CO_2 and O_2 are identified to emanate from the electrolyte–cathode interface at charging potentials > 3.8 V (vs Li/Li^+). The gas evolution is correlated with a large increase in cathode interfacial resistance observed by potential-resolved impedance spectroscopy. This is the first evidence of electrochemical decomposition of interfacial Li_2CO_3 in garnet cells and suggests a need to report “time-to-assembly” for cell preparation methods.

1. Introduction

Solid state lithium-ion batteries offer several advantages over traditional lithium-ion batteries, most notably in enhanced safety and energy density, making them ideal for applications such as electric vehicles. However, these devices encounter stability issues with cycling, and viable commercial implementation will require a better understanding of their degradation mechanisms. The garnet $Li_7La_3Zr_2O_{12}$ (LLZO) is one of the most promising solid electrolytes owing to its high conductivity and stability versus Li metal. However, it is known to form an insulating Li_2CO_3 surface layer upon exposure to H_2O and CO_2, decreasing its efficacy. Formation of Li_2CO_3 is proposed to proceed in a two-step process, mediated by LiOH:[1]

$$Li_7La_3Zr_2O_{12} + xH_2O \rightarrow Li_{7-x}H_xLa_3Zr_2O_{12} + xLiOH \tag{1}$$

$$LiOH + 1/2CO_2 \rightarrow 1/2Li_2CO_3 + 1/2H_2O \tag{2}$$

Further mechanistic details of the formation of these layers, along with methods of characterization and impacts on interfacial phenomena such as Li-dendrite growth on anodes, have been recently reviewed, with a focus on “best practices” for eliminating Li_2CO_3.[2] To minimize contamination, the current state-of-the-art synthesis procedure for “clean” LLZO involves polishing the electrolyte and annealing above 400 °C, completely within an inert argon atmosphere. However, even going beyond this with rigorous ultra-high vacuum heat treatments, it has been found that these contaminants gradually reform at room temperature in an argon glovebox.[3]

Here we present direct evidence linking Li_2CO_3 to interfacial delamination between a model cathode and LLZO, assembled according to current standard practices. We implement operando electrochemical mass spectrometry (EC-MS) to show decomposition of sub-nanometer layers of Li_2CO_3 during charging cycles. These deposits (re)form on the surface of the LLZO between the time of its annealing and deposition of the cathode. The decomposition causes irreversible degradation of contact between the cathode and LLZO, and is a direct consequence of the oxidation of Li_2CO_3:[4]

$$Li_2CO_3 \rightarrow 2Li^+ + 2e^- + 1/2O_2 + CO_2 \left(E^0 = 3.82V \text{ vs } Li/Li^+\right) \tag{3}$$

We show these effects using thin-film LMO|LLZO|Li cells (LMO = $LiMn_2O_4$) and leverage potential-resolved electrochemical impedance spectroscopy (PR–EIS) as a complimentary method to highlight how these changes affect charge transport through the system. Gas evolution is further found to occur when applying a charging current to Au|LLZO|Li cells, where the gold acts as an ion-blocking electrode; this highlights that

Dr. A. A. Delluva, J. Kulberg-Savercool, Prof. A. Holewinski
Department of Chemical and Biological Engineering
University of Colorado
Boulder, CO 80309, USA
E-mail: adam.holewinski@colorado.edu
Dr. A. A. Delluva, Prof. A. Holewinski
Renewable and Sustainable Energy Institute
University of Colorado
Boulder, CO 80309, USA
Prof. A. Holewinski
Materials Science and Engineering Program
University of Colorado
Boulder, CO 80309, USA

The ORCID identification number(s) for the author(s) of this article can be found under https://doi.org/10.1002/adfm.202103716.

DOI: 10.1002/adfm.202103716

the decomposition reaction is interface-specific, rather than the result of carbonate formation on the surface of the cathode material.

To our knowledge, carbonate-induced delamination has not previously been observed or quantified for solid-state Li-ion batteries prepared by current best practices. We suggest this is because the primary focus of the field has been on engineering of the Li–metal anode interface[5–10] (and largely using symmetric cells), which operate near 0 V, whereas we observe the effect at an onset overpotential above 3.8 V. It is a problem specific to the cathode interface, and one that possibly explains the common observation of large, unsustained first-cycle charging capacities seen for solid-state Li-ion batteries. Broadly, our investigations demonstrate an operando methodology for assessing the interfacial quality of assembled cells, and they suggest the necessity of highly controlled synthesis conditions to create effectively-contaminant-free garnet electrolyte cells. These findings have particular implications in limitations for fast charging and high-voltage cathodes, which we suggest will require investigation for correlations between gas evolution and performance shifts as a future standard practice.

2. Results and Discussion

To characterize the cathode interface evolution of LLZO-based solid-state cells, a thin film architecture, Li|LLZO|LMO, with sputter-deposited LMO cathodes was employed (Figure S1, Supporting Information). This architecture enables cell cycling without the use of binders and conductive additives that could present spurious sources of carbon. Prior to assembly, electrolyte powders were pelletized, then calcined and sintered at 1200 °C. Thermogravimetric analysis–mass spectrometry curves are shown in Figure S2, Supporting Information, illustrating the loss of any residual carbon well below the maximum temperature, and X-ray diffraction patterns before and after calcination are also presented in Figure S3, Supporting Information, showing no detectable Li_2CO_3. Electrolyte pellets were kept under argon at all times leading up to cathode deposition, and immediately before sputtering, the electrolytes were polished and annealed in argon at 400 °C (as has been established to remove surface carbonates[2]). The sputtered LMO films were found to be amorphous, but chemical analysis using EDS and Raman spectroscopy confirm appropriate stoichiometry and vibrational characteristics (Figures S4 and S5, Supporting Information). The exact nature of the cathode is not critical to the study of electrolyte-based contamination—it only needs to be carbon-free. The "time-to-assembly" (post-annealing) was roughly 3–5 h for these standard cells.

During initial cycling, large first-cycle charging capacities were observed, followed by much smaller subsequent discharge capacities, as shown in **Figure 1**. Alongside the initial losses in capacity, the coulombic efficiencies of these cells showed a marked increase and gradual stabilization (at the diminished capacity) as cycling continued. Reports of high-charging capacities and subsequent capacity fade for the first cycles of bulk-type LLZO full cells have previously been ascribed to organolithium compounds formed during sintering.[11–13] However, these compounds have never been identified, and while they are likely present in the cited systems (likely alongside Li_2CO_3), they would not be present in the cells constructed in this study because the cathodes here were not derived from organic precursors.

To explore the nature of the initial degradation effects, impedance response was next monitored throughout early charging and discharging cycles to probe the potential–dependence of characteristic microscopic processes. A full cycle corresponds roughly to variation of the lithium stoichiometry in the range $0 < x < 2$ for $Li_{2-x}Mn_2O_4$. To identify onset regimes of various phenomena, the charging cutoff voltage was increased between sequential cycles while taking the PR–EIS measurements. **Figure 2**A,B shows EIS taken at intervals of 400 mV between initial charge and discharge cutoffs of 4 and 2 V versus Li/Li$^+$, respectively. We have previously resolved these spectra into a number of bulk and interfacial contributions through comparison with symmetric cells (Li–Li, LMO–LMO, and blocking Au–Au), and found that a mid-frequency semicircle preceding the low-frequency diffusion tail corresponds to the parallel processes of charge transfer and space charge formation at the LMO|LLZO interface.[14] An equivalent circuit diagram and detailed fits will be discussed below, but we first comment on

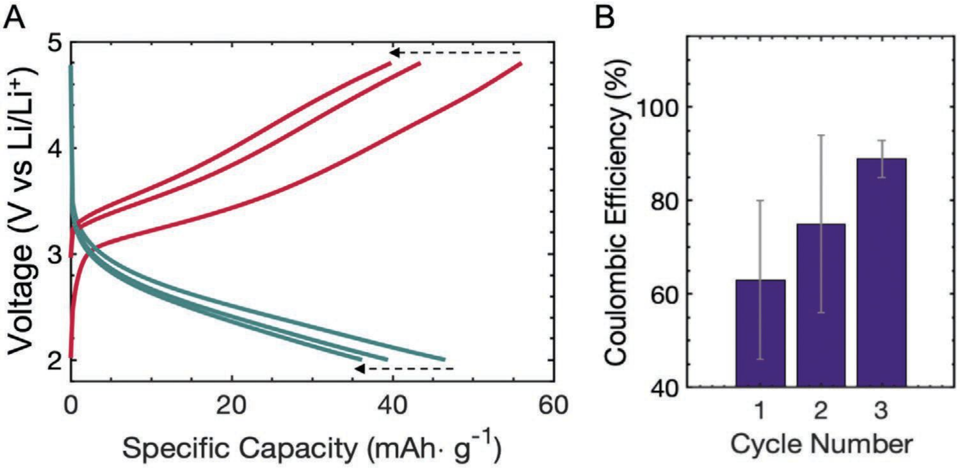

Figure 1. A) Representative charge (red) and discharge (teal) behavior over three cycles for LMO|LLZO|Li cells. B) Average coulombic efficiencies based on three replicate cells over three cycles for LMO|LLZO|Li architecture. Cells were cycled at 38 uA cm^{-2} (≈3C).

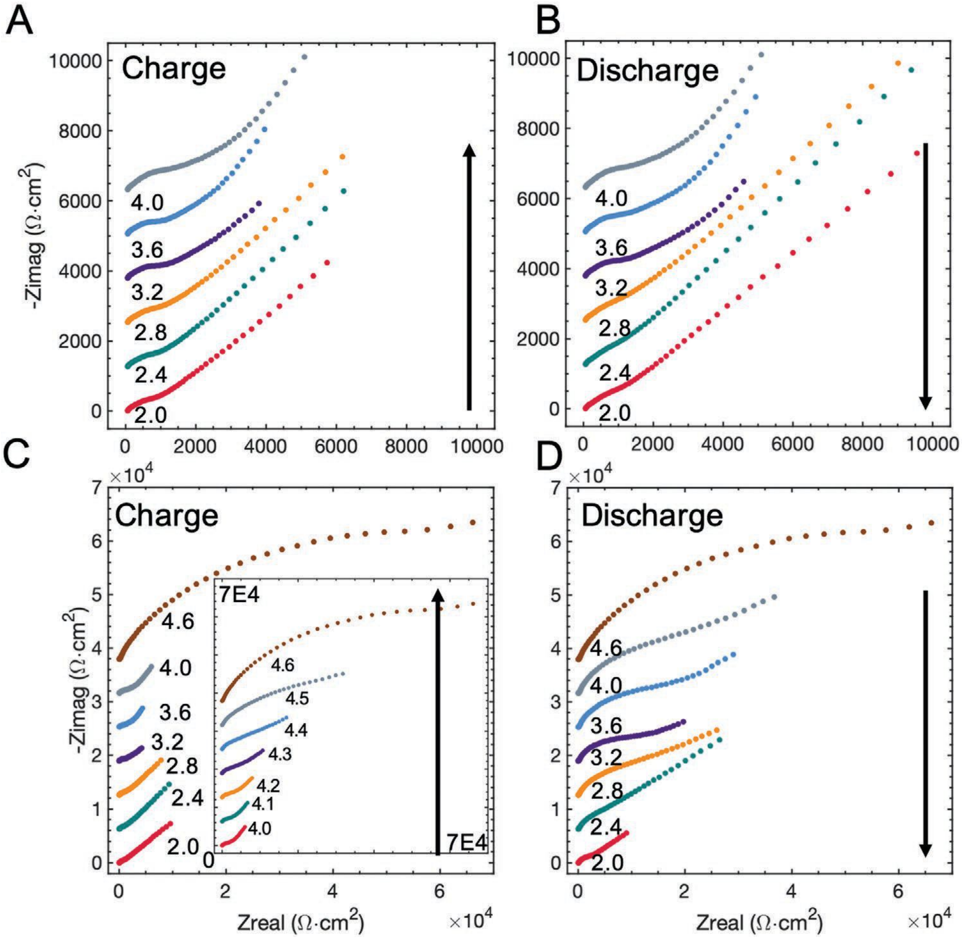

Figure 2. Potential resolved impedance spectra for LMO|LLZO|Li cells. A,B) Spectra for charge and subsequent discharge with 4.0 V cutoff. C,D) Spectra for charge and subsequent discharge with 4.6 V cutoff showing irreversible degradation at the higher potential. Inset in panel (C) shows every 100 mV between 4 and 4.6. Frequencies range from 1 MHz to 0.5 Hz (left to right across each spectrum.) The rate of cycling between EIS measurements was ≈C/3 (3.8 μA cm^{-2}).

a few holistic aspects. Most importantly, when kept below 4 V, the primary features of the EIS response appear to maintain their relative magnitude and shape at individual voltages in either cycling direction, with the exception of a slight growth in resistance associated with the diffusion regime (crystal domain growth within the thin film).[15] In contrast, when the cutoff voltage is increased, the mid-frequency impedance arc associated with interfacial charge transfer at the cathode grows to a dramatically larger resistance that persists throughout the remainder of the EIS measurements over discharge and further cycling. Figure 2C,D shows a survey of PR–EIS spectra between a high charge cutoff of 4.6 V and discharge back to 2 V, with finer spacings of 100 mV shown in the inset of Figure 2C. Clear changes in the EIS signatures manifest around 4.3–4.4 V. While this is a relatively high voltage of apparent onset, it may be noted that CO$_2$ evolution (to be shown below) is observed much sooner (3.8 V) and simply accelerates at higher voltage. This suggests that the same degradation mechanism may be subtly operative in many cells within the literature that uses a cutoff voltage of 4.0 V, despite it not resulting in obvious, large, single-cycle impedance increases.

The physicochemical changes induced by decomposition of Li$_2$CO$_3$ can be further compared in equivalent circuit (**Figure 3**C) fits for the EIS before and after high charging voltages were applied to the cell (Figure 3A,B). The fits after high voltage charging (4th half-cycle) show a large increase to the interfacial resistance of the cathodic interface arc (R_{LMO}) as may be expected, as well as a noticeable decrease in the associated constant phase element (CPE) exponent (n_{LMO}) (Figure 3E; full fitting data in Table S1, Supporting Information). CPEs are used to model the non-ideality of real electrochemical capacitances, and a decrease in the exponent can be indicative of increasing surface roughness,[16] such as would be the case for a previously sharp LMO|(Li$_2$CO$_3$)|LLZO interface that was experiencing delamination. In addition to the changes in the parameters characterizing the cathode interface itself, it may be noted that the time constant associated with diffusion within the LMO also rises. The time constant relates to both the diffusion coefficient and the characteristic path length $\left(\tau_{\mathrm{d}} = \frac{\delta^2}{D_x^{\alpha}}\right)$, and the initial diffusion coefficient (estimating δ as electrode thickness) was 1.01×10^{-10} cm^2 s^{-1}, in relative agreement with literature.[17,18]

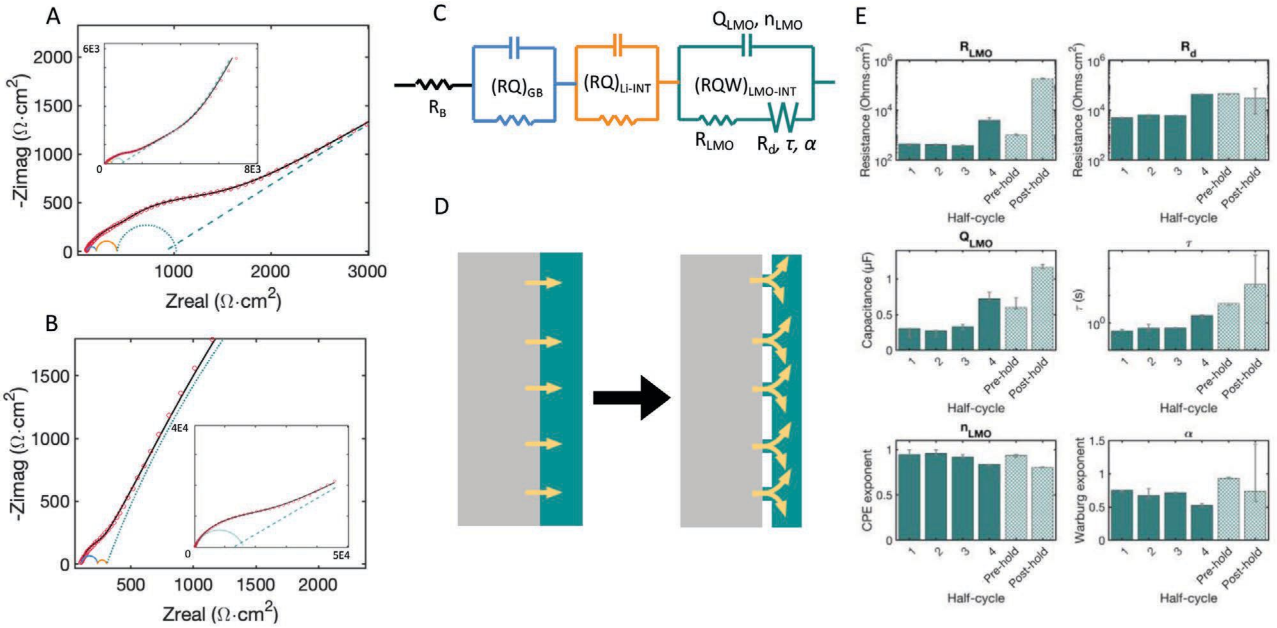

Figure 3. EIS analysis of LMO|LLZO|Li cells. A) EIS spectra and fit component impedances measured at 3.6 V, before high voltage was applied. B) EIS spectra and fit component impedances measured at 3.6 V, after high voltage was applied. A large growth in the final semicircle feature is evident. C) Equivalent circuit used to fit LMO|LLZO|Li cells, with elements involving critical parameters marked. D) Sketch showing the relation between delamination and increased path lengths for diffusion in the cathode. E) Evolution of the labeled equivalent circuit parameters corresponding to the teal section of the circuit (equations in Supporting Information) measured at 3.6 V over four half-cycles 2.0–4.6 V (labeled 1–4), as well as before and after more extreme cycling (with a fresh cell, light hatched bars) including a 10 min potentiostatic hold at 4.8 V. All error bars represent 95% confidence intervals determined by bootstrap Monte Carlo error sampling, described in the Supporting Information.

After applying high voltage, we attribute the rise in τ_d to increases in the average diffusion path length for Li entering the film at fewer points, due to delamination (see sketch in Figure 3D). Similar increases are not seen (or expected) in the resistance associated with LLZO due to the much large aspect ratio of the electrolyte pellet in comparison to delamination regions (i.e., the average path length for Li in the electrolyte changes marginally after delamination). The interpretation with regard to increased path lengths in the cathode phase is also consistent with the changes seen in the finite Warburg element resistance (R_d), which we previously mentioned relates more directly to grain growth; the key distinction to stress in comparison to τ_d is that the changes to R_d are more asymptotic with respect to cell break-in. Figure 3E highlights this through comparison of separate tests on an identical cell subjected to more extreme cycling to a 4.8 V cutoff and a potentiostatic hold at 4.8 V (the procedure utilized below for gas quantification; EIS in Figure S6, Supporting Information, fits in Table S2, Supporting Information). After the higher voltage hold, the area-specific resistance for the Warburg element (R_d) still plateaus on the order of 10^5 Ω cm^2, whereas the R_{LMO} and τ_d values, attributed to Li_2CO_3 decomposition, show much more growth relative to their initial values, beyond what occurred in the 4.6 V cycled cells.

The observed irreversible growth in interfacial impedance could in principle be consistent with either physical delamination (instigated by Li_2CO_3 decomposition) or chemical reaction (between cathode and electrolyte). This was probed by using Au cathodes in place of LMO. Because Au is a blocking electrode, appreciable charging of the cell should not be possible in the absence of any surface contaminants. However, a small irreversible charging current was able to be passed, thereby suggesting the presence of an unstable impurity phase at the Au–LLZO interface. The EIS of the Au|LLZO|Li cells before and after this irreversible charge (Figure S7, Supporting Information) also shows over an order of magnitude increase in the resistance associated with the Au–LLZO interface (Table S3, Supporting Information). This corroborates the suggestion of a mechanism for delamination via the electrochemical oxidation of Li_2CO_3, re-formed before the cathode is deposited. Further fitting details are provided in the Supporting Information.

Differential electrochemical mass spectrometry (DEMS) has previously been implemented to quantitatively assess the stoichiometry and Faradaic (in)efficiency toward Li_2CO_3 in traditional (liquid–electrolyte) Li-ion batteries,[19–21] as well as other systems requiring detailed accounting of charge passed, such as Li–O_2 batteries.[22,23] However, in solid-state cells with proper pretreatments according to current best practices, the amount of Li_2CO_3 available to be oxidized at the LMO–LLZO interface is very low, and its ability (or timescale) to escape the buried solid–solid interface is also unknown. Special care was thus taken in designing a cell and EC–MS system with adequate sensitivity to detect low amounts of gas that would be associated with electrochemical decomposition of re-formed Li_2CO_3. As a point of reference, a 1 nm thick film would correspond to ≈2 nmol of crystalline Li_2CO_3 per cm^2 of LLZO pellet. A custom low headspace volume (≈300 µL) housing (Figure S8A, Supporting Information) was thus constructed for the LMO|LLZO|Li cells to interface with the EC–MS apparatus (Figure S8C, Supporting Information). Calibration details for the quantification of the

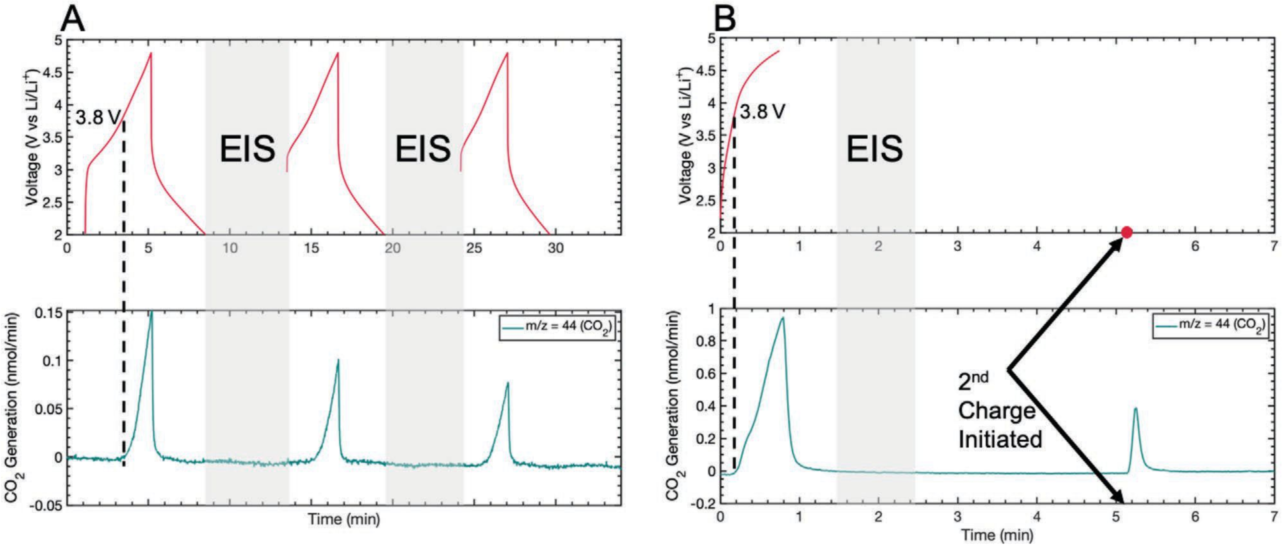

Figure 4. Evolution of CO_2 detected by EC–MS and correlated to cell voltage while cycling. A) Evolution over three cycles for LMO|LLZO|Li cell. B) Evolution over two cycles for Au|LLZO|Li cell, after which the cell was inoperable. The onset potential of gas evolution is highlighted for the first cycle in each case. LMO and Au cells were cycled at 38 uA cm^{-2} (≈3C for the LMO cells).

rates of gas evolution are presented in Figure S9, Supporting Information.

Using the low-volume cell and EC–MS apparatus, cells were first discharged to 2V before initiating a cycling procedure from 2.0–4.8 V. As the cell charged, CO_2 (**Figure 4**A) and O_2 (Figure S10A, Supporting Information) evolution was detected at ≈3.8 V and above. No gas evolution was detected during discharge; however, evolution of both O_2 and CO_2 resumed on the following two charging cycles, with diminishing response each time, consistent with degradation of a finite source of Li_2CO_3.[24] The total amount of CO_2 evolved based on these first three cycles followed by a 10 min potentiostatic hold at 4.8 V (full profile in Figure S11, Supporting Information) totaled 0.51 nmol, which would correspond to an ≈0.2 nm film, if the entire interfacial quantity of Li_2CO_3 was decomposed. Some uncertainty exists in the possibility of electrically isolating material prior to decomposition, which is discussed further below. Currently, there are only two examples of MS being employed to monitor all-solid-state cells during operation, and these works involved measuring the evolution of CO_2 from bulk cathodes.[25,26] Thus, the current work represents identification of a new "chemically relevant" lower limit for Li_2CO_3 contamination, specific to the interfacial characteristics of solid-state systems.

Further verification of interfacial Li_2CO_3 decomposition was demonstrated by applying oxidative currents to Au|LLZO|Li cells while monitoring gas evolution by EC–MS. Both CO_2 (Figure 4B) and O_2 (Figure S10B, Supporting Information) were observed, and the cell was found to be effectively dead after the first cycle—initiating the same oxidation procedure a second time immediately hit the cutoff voltage of the experiment. The total evolution from the Au cell amounted to 0.38 nmol of CO_2, similar to the LMO cell, but in contrast, the first cycle gave a much higher rate of CO_2 evolution. We hypothesize that gas trapping within interfacial pockets could provide an underestimate of the CO_2 produced, and this may be more prevalent in the LMO cells due to better adhesion between regions in direct contact with LLZO, as well as the electrode thickness (LMO + Al ≈230 nm vs Au ≈80 nm). We note that when studying contamination, exact quantities will inherently be subject to variation; the magnitudes of carbon evolution quoted here are reproducible within our procedure and are meant to be representative of typical preparations considered to be standard best practices in most labs. Using a sputter chamber equipped with a substrate heater capable of annealing the LLZO pellets under UHV conditions directly prior to deposition could likely synthesize a truly Li_2CO_3-free surface; however, the key takeaway is that for typical assembly conditions that require exposure to a glovebox environment, vanishingly small quantities of Li_2CO_3 still have a substantive impact.

To gain some insight into the effect of exposure time, a series of Au cells were constructed with varying times between carbonate removal and deposition (Figure S12, Supporting Information). It was found that for cells with shorter exposure times, more charge was actually able to be passed before cell failure. This trend indicates that as cells build up a carbonate layer, the decomposition-induced delamination can be accelerated and not all carbonate present will decompose before becoming electrically isolated. This suggests that quantification of off-gassing on cells assembled with the lowest amounts of carbonate will provide more accurate estimates than more poorly synthesized (contaminated) cells. We suspect the impact of premature delamination (before total carbonate decomposition) is more pronounced on the Au blocking cells than for LMO cathodes, but nonetheless it is a challenge in obtaining true quantification.

3. Conclusion

Through cycling and PR–EIS measurements of electrochemical cells with LLZO electrolytes, we observed a large resistive feature that corresponds with changes to the LLZO–cathode interface. This change becomes prominent in the 4–4.5 V cell potential range. Through the use of operando EC–MS, we found evidence for the electrochemical decomposition of Li_2CO_3 coinciding with these changes, with gas evolution onsetting at even lower potentials than where major short-term performance losses are observed. By using comparable cells with insertion and blocking electrodes, we were able to confirm that gas evolution was specifically from the cathode interface. The changes observed here are generally not observed in Li symmetric cells, where the voltages are lower, and thus we underscore the importance of full cell testing when designing synthesis methods for garnet solid electrolyte-based batteries. Lithium carbonate decomposition will be a particular concern for high voltage and fast-charge cathode materials, which may experience more rapid and catastrophic failure by this mechanism. We have further demonstrated that while removal of electrolyte-based lithium carbonate is extremely important, post-removal cell assembly must also be viewed as time-sensitive even in argon glovebox conditions, demanding additional strategies to prevent surface contaminant re-formation.

While the thin film cells studied here are most effective in isolating the impact of interfaces, further research will be needed to determine how the findings of this study translate to bulk-cathode cells. We suspect that the negative effects of delamination might be reduced if a more integrated, 3D interface is formed (e.g., graded cathodes), but because the decomposition reaction stems from the electrolyte, it will still pose an issue unless formation of Li_2CO_3 can be completely mitigated. Extremely rapid cell assembly and/or assembly of solid-state cells under inert atmospheres at temperatures >400 °C could be one pathway to forming a Li_2CO_3-free interface, but this would be contingent upon avoiding interfacial reactions possibly taking place between electrolyte and electrode at these elevated temperatures. Sequential sputtering has been recently employed to this effect to create LCO|LLZO half cells,[27] though the approach would not readily be adapted beyond thin film batteries. Furthermore, it is possible that protective interlayers,[12,28] if fabricated quickly, could help mitigate this issue by shielding LLZO from contaminants.[29] No matter which direction these Li_2CO_3 mitigation routes take, increased attention to detail and documentation of synthesis conditions including time-to-assembly and gaseous environment conditions at all stages for each electrode—ideally followed by in situ analyses of off-gassed products—will be necessary to accurately probe the degradation mechanisms of LLZO-containing cells.

4. Experimental Section

Electrolyte Preparation: $Li_{6.4}La_3Zr_{1.4}Ta0_{.6}O_{12}$ (LLZTO) was purchased from MTI Corporation (μ_d = 5 µm) and pelletized in a 13 mm stainless steel die (Across International) in 1 g increments at 2 MT of pressure using a mechanical press (Carver Model M). The resulting pellets were placed in MgO boats within a tube furnace (Thermcraft XST-3-0-36-1V2-F01) for a two-step sintering process,[30] which has been shown to help densify pellets while limiting lithium loss through an initial high temperature nucleation step and then lower temperature grain growth. Pellets were initially heated to 1200 °C at a ramp rate of 3 °C min^{-1} and held for 1 h. The temperature was then reduced to 1100 °C and held for 5 h before cooling to room temperature at a rate of 100 °C h. The approximate density of the pellets was 90%. Faces of the pellets were polished in air progressively with 150, 400, 800, and 1000 grit sandpapers (3M, proprietary ceramic), followed by wet polishing with 1, 0.3, and 0.05 µm alumina particles (Electron Microscopy Sciences) to ensure a flat surface for electrode deposition as well as reduce Li_2CO_3 contamination.[31] The resulting pellet thicknesses were roughly 1.5 mm. Pellets were then immediately transferred into an argon filled glovebox and heated to 400 °C for 3 h to remove residual Li_2CO_3 prior to cathode deposition.

Cathode Deposition: For LMO electrodes, pellets were next transferred under argon to an RF-sputtering deposition chamber (via a vacuum desiccator with pump, Desi–Vac) built within an argon-filled glove box (Angstrom Engineering). LMO electrodes were deposited from a 2" LMO target (99.9% purity, ACI Alloys, Inc.). The sputter deposition was carried out at 60 W, 15 cm target distance, 15 sccm of argon flow. A stainless-steel shadow mask with 10 mm diameter circles was used to control where the deposition occurred on the LLZO pellets. Depositions were 2 h per electrode, with an estimated deposition rate of 0.9 nm min^{-1} to a total thickness of 110 nm. Aluminum current collectors were deposited within the same deposition chamber from an aluminum target to a thickness of ≈120 nm, making the total thickness of cathode and current collector ≈230 nm. The cathode/electrolyte pellets were then transferred under argon back to the original glovebox for cell assembly. The estimated time between cooling of LLZO pellets and final cathode deposition was 3–5 h.

For Au electrodes, pellets were transferred under argon to a thermal evaporation chamber built within a nitrogen-filled glovebox (Angstrom Engineering). Gold pellets (Kurt J. Lesker Company) were evaporated using a two-step deposition process to a thickness of 80 nm. The gold films were transferred under nitrogen back to the original argon glovebox and annealed at 200 °C to improve adhesion of the evaporated films. The estimated time between cooling of LLZO pellets and cathode deposition was ≈3–4 h.

Cell Assembly and Testing: (MBRAUN Unilab Pro SP). To create the full cells, lithium foils. (0.75 mm thick) were punched (10 mm diameter), scraped to remove oxide, pressed onto the LLZO pellet, and placed into customized Swagelok cells (Figure S4A, Supporting Information). The side of the LLZO pellet opposite the LMO was gently polished with 2000 grit sandpaper inside the glovebox prior to cell assembly to re-clean the interface. The cells were then heated to 100 °C under 36 kPa pressure, the lithium foil separated and re-scraped to remove any newly-formed lithium oxide, and re-adhered to the LLZO. It was found that an oxide forms on the surface of the lithium if a high pressure is not immediately applied across these cells, due to trace oxygen diffusing to the interface, but scraping and pressing at 100 °C forms a protected interface.[10] This re-scraping procedure was found to decrease the Li–LLZO interfacial impedance substantially and thus improve resolution of other impedance features. These pellet stacks were placed within PEEK cells, clamped in a vice to apply stack pressure, and rapidly connected to the MS for electrochemical testing at 100 °C. Calibration of cell headspaces for CO_2 was performed with standard calibration gases (GASCO); the O_2 response was too near baseline to quantify.

All electrochemical measurements were performed on a Bio-logic SP-300 potentiostat/galvanostat/FRA. Prior to all reported cycling data, LMO cells were discharged to 2 V at a rate of ≈C/10 (to ensure cells started in fully discharged state). The theoretical capacity of all LMO cells was estimated to be 10.2 µAh, based on the thickness of the electrodes and the complete extraction of two full units of lithium (285 mAh g^{-1}). Some variation in cell capacities was expected due to variations in current collector contact resulting from use of a rigid vice piston for pressure (see Section S1, Supporting Information). The areal loadings of the cathodic and anodic current collectors were 0.045 mg cm^{-2}. The resulting excess capacity of the lithium electrode relative to the LMO cathode was thus ≈13 000×.

Supporting Information

Supporting Information is available from the Wiley Online Library or from the author.

Acknowledgements

This work was funded by NSF CBET #1806059. The COSINC-CHR at CU Boulder was utilized for characterization. The authors acknowledge Jessica Dudoff, Dr. Chaiwat Engtrakul, and the National Renewable Energy Lab for assistance in synthesis of the LMO cathodes.

Conflict of Interest

The authors declare no conflict of interest.

Data Availability Statement

The data that supports the findings of this study are available in the supplementary material of this article.

Keywords

electrochemical mass spectrometry, lithium carbonate, lithium ion batteries, solid electrolytes, solid interface, solid state batteries

Received: May 20, 2021

---

[1] A. Sharafi, S. Yu, M. Naguib, M. Lee, C. Ma, H. M. Meyer, J. Nanda, M. Chi, D. J. Siegel, J. Sakamoto, *J. Mater. Chem. A* **2017**, *5*, 13475.
[2] H. Huo, J. Luo, V. Thangadurai, X. Guo, C. W. Nan, X. Sun, *ACS Energy Lett.* **2020**, *5*, 252.
[3] Y. Zhu, J. G. Connell, S. Tepavcevic, P. Zapol, R. Garcia-Mendez, N. J. Taylor, J. Sakamoto, B. J. Ingram, L. A. Curtiss, J. W. Freeland, D. D. Fong, N. M. Markovic, *Adv. Energy Mater.* **2019**, *9*, 1803440.
[4] N. Mahne, S. E. Renfrew, B. D. McCloskey, S. A. Freunberger, *Angew. Chem., Int. Ed.* **2018**, *57*, 5529.
[5] A. Sharafi, H. M. Meyer, J. Nanda, J. Wolfenstine, J. Sakamoto, *J. Power Sources* **2016**, *302*, 135.
[6] M. J. Wang, R. Choudhury, J. Sakamoto, *Joule* **2019**, *3*, 2165.
[7] T. Krauskopf, H. Hartmann, W. G. Zeier, J. Janek, *ACS Appl. Mater. Interfaces* **2019**, *11*, 14463.
[8] C. Ma, Y. Cheng, K. Yin, J. Luo, A. Sharafi, J. Sakamoto, J. Li, K. L. More, N. J. Dudney, M. Chi, *Nano Lett.* **2016**, *16*, 7030.
[9] Y. Lu, X. Huang, Y. Ruan, Q. Wang, R. Kun, J. Yang, Z. Wen, *J. Mater. Chem. A* **2018**, *6*, 18853.
[10] H. Zheng, S. Wu, R. Tian, Z. Xu, H. Zhu, H. Duan, H. Liu, *Adv. Funct. Mater.* **2019**, *30*, 1906189.
[11] K. J. Kim, J. L. M. Rupp, *Energy Environ. Sci.* **2020**, *13*, 4930.
[12] F. Han, J. Yue, C. Chen, N. Zhao, X. Fan, Z. Ma, T. Gao, F. Wang, X. Guo, C. Wang, *Joule* **2018**, *2*, 497.
[13] S. Ohta, S. Komagata, J. Seki, T. Saeki, S. Morishita, T. Asaoka, *J. Power Sources* **2013**, *238*, 53.
[14] A. A. Delluva, J. Dudoff, G. Teeter, A. Holewinski, *ACS Appl. Mater. Interfaces* **2020**, *12*, 24992.
[15] J. B. Bates, N. J. Dudney, B. Neudecker, A. Ueda, C. D. Evans, *Solid State Ionics* **2000**, *135*, 33.
[16] M. E. Orazem, N. Pábre, B. Tribollet, *J. Electrochem. Soc.* **2006**, *153*, 129.
[17] S. B. Tang, M. O. Lai, L. Lu, *Mater. Chem. Phys.* **2008**, *111*, 149.
[18] N. Kuwata, M. Nakane, T. Miyazaki, K. Mitsuishi, J. Kawamura, *Solid State Ionics* **2018**, *320*, 266.
[19] H. Wang, E. Rus, T. Sakuraba, J. Kikuchi, Y. Kiya, H. D. Abruna, *Anal. Chem.* **2014**, *86*, 6197.
[20] S. E. Renfrew, B. D. McCloskey, *ACS Appl. Energy Mater.* **2019**, *2*, 3762.
[21] E. Castel, E. J. Berg, M. El Kazzi, P. Novák, C. Villevieille, *Chem. Mater.* **2014**, *26*, 5051.
[22] M. M. O. Thotiyl, S. a. Freunberger, Z. Peng, P. G. Bruce, *J. Am. Chem. Soc.* **2013**, *135*, 494.
[23] B. D. McCloskey, D. S. Bethune, R. M. Shelby, T. Mori, R. Scheffler, a Speidel, M. Sherwood, a C. Luntz, *J. Phys. Chem. Lett.* **2012**, *3*, 3043.
[24] Y. Li, X. Chen, A. Dolocan, Z. Cui, S. Xin, L. Xue, H. Xu, K. Park, J. B. Goodenough, *J. Am. Chem. Soc.* **2018**, *140*, 6448.
[25] F. Strauss, J. H. Teo, A. Schiele, T. Bartsch, T. Hatsukade, P. Hartmann, J. Janek, T. Brezesinski, *ACS Appl. Mater. Interfaces* **2020**, *12*, 20462.
[26] T. Bartsch, F. Strauss, T. Hatsukade, A. Schiele, A. Y. Kim, P. Hartmann, J. Janek, T. Brezesinski, *ACS Energy Lett.* **2018**, *3*, 2539.
[27] J. Sastre, X. Chen, A. Aribia, A. N. Tiwari, Y. E. Romanyuk, *ACS Appl. Mater. Interfaces* **2020**, *12*, 36196.
[28] Y. Xiao, L. J. Miara, Y. Wang, G. Ceder, *Joule* **2019**, *3*, 1252.
[29] J. F. Wu, B. W. Pu, D. Wang, S. Q. Shi, N. Zhao, X. Guo, X. I.n Guo, *ACS Appl. Mater. Interfaces* **2019**, *11*, 898.
[30] X. Huang, T. Xiu, M. E. Badding, Z. Wen, *Ceram. Int.* **2017**, *44*, 5660.
[31] A. Sharafi, E. Kazyak, A. L. Davis, S. Yu, T. Thompson, D. J. Siegel, N. P. Dasgupta, J. Sakamoto, *Chem. Mater.* **2017**, *29*, 7961.